Energy-transfer and charge-separation pathways in the reaction center of photosystem II revealed by coherent two-dimensional optical spectroscopy

Darius Abramavicius[a)] and Shaul Mukamel[b)]

Department of Chemistry, University of California, Irvine, Irvine, California 92697-2025, USA

The excited state dynamics and relaxation of electrons and holes in the photosynthetic reaction center of photosystem II are simulated using a two-band tight-binding model. The dissipative exciton and charge carrier motions are calculated using a transport theory, which includes a strong coupling to a harmonic bath with experimentally determined spectral density, and reduces to the Redfield, the Förster, and the Marcus expressions in the proper parameter regimes. The simulated third order two-dimensional signals, generated in the directions $-\mathbf{k}_1+\mathbf{k}_2+\mathbf{k}_3$, $\mathbf{k}_1-\mathbf{k}_2+\mathbf{k}_3$, and $\mathbf{k}_1+\mathbf{k}_2-\mathbf{k}_3$, clearly reveal the exciton migration and the charge-separation processes. © 2010 American Institute of Physics. [doi:10.1063/1.3493580]

I. INTRODUCTION

Charge separation in the core of pigment-protein reaction-center (RC) complexes is the first energy conversion step in photosynthesis. The subsequent electron transfer across a thylakoid membrane of chloroplasts triggers a proton transfer reaction, creating a charge gradient that drives a chain of chemical reactions, leading eventually to the stable storage of solar energy.[1] Photosystem II (PS-II), which is the most abundant photosynthetic complex in Nature,[2] is responsible for water splitting. Its 2.9 Å resolution RC structure shows two branches of pigments, D1 and D2, each made up of two chlorophyll molecules (Chl) and one pheophytin (Phe), and other pigments that are separated from these six core pigments either energetically or spatially.[3] All six chromophores are tightly packed within an $\sim 30^3$ Å^3 volume and show strong (50–200 cm^{-1}) resonant exciton interactions.

The Frenkel exciton model has often been used to describe collective electronic excitations in molecular complexes.[4] This model and the system-bath coupling has been parametrized for PS-II by Raszewski *et al.* using a numerical optimization algorithm, which yields good agreement with linear optical properties.[5] A more elaborate spectral density of the system-bath coupling was used by Novoderezhkin *et al.*[6] by employing 48 vibrational bath modes extracted from low-temperature fluorescence line-narrowing data. The extended model includes charge transfer (CT) states coupled to other molecular excitations. It can adequately describe absorption, fluorescence, and Stark spectrum, which depend only on singly excited states. Despite the extensive studies of electron separation and transfer time scales, the primary charge-separation site in PS-II RC is still not clearly identified: several radical pair (RP) evolution scenarios fit the existing experiments.[7] The model parameters were refined[6] by including fluorescence and Stark spectroscopy data. The strong dependence of the Stark spectrum on CT states helped determine some of the parameters.

The absorption spectrum is not very sensitive to the CT states. This is to be expected since the isolated CT states carry no oscillator strength from the ground state. This selection rule is broken by mixing the CT with the Frenkel exciton states, leading to a weak absorption of the CT state. Due to large static dipole of a CT state, the Stark spectrum is sensitive to electron transfer. However, for the same reason, CT states are strongly coupled to the medium causing large broadening, which makes them harder to resolve.

An optical excitation creates an electron-hole pair localized on the same chromophore. In the CT state, they reside on different molecules. Charge separation from a molecular excited state corresponds to a quantum transition between a molecular excited state and a CT state. The above phenomenological hybrid (Frenkel+CT exciton) model misses some characteristics of CT states, such as electron-hole Coulomb interaction, electron affinities, and ionization energies, as well as fermionic properties of electrons and holes. Therefore, it cannot be directly used to compute double-exciton states.

In this paper, we develop a tight-binding two-band model for the core RC complex of PS-II and use it to simulate the energy-transfer and charge-separation dynamics. We account for strong CT state coupling with the bath by using a modified Redfield rate expression for the energy and charge hopping, which treats diagonal fluctuations nonperturbatively.[8] Closed expressions are derived for the third order optical signals with Gaussian lineshapes that account for static inhomogeneities of the system without the need to sample the ensemble realizations explicitly. The signatures of CT states in various two-dimensional (2D) optical signals are identified.

---

a)Electronic mail: darius.abramavicius@ff.vu.lt.
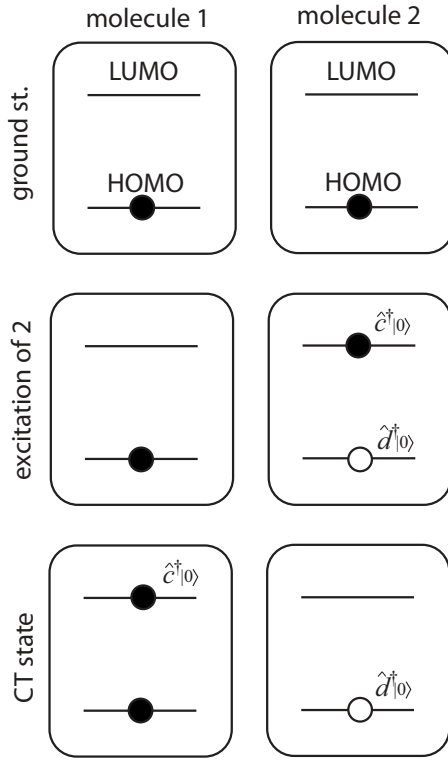b)Electronic mail: smukamel@uci.edu.

FIG. 1. Tight-binding model of molecular aggregates. Two molecules are shown. First row: the ground $|0\rangle$ state. Second row: excitation of molecule 2 corresponds to creation of hole and electron on that molecule. Third row: CT state corresponds to creation of hole on molecule 2 and an electron on molecule 1. Electrons are marked by solid circles and holes by open circles.

II. TIGHT-BINDING TWO-BAND HAMILTONIAN FOR EXCITON AND CHARGE-TRANSFER DYNAMICS

We consider an aggregate where each chromophore has two frontier orbitals: the highest occupied molecular orbital (HOMO) and the lowest unoccupied molecular orbital (LUMO).[9] Neglecting spin, each chromophore then has four states: the ground state $|0\rangle$, where the HOMO is occupied and the LUMO is not; the negatively charged electron state $\hat{c}_m^\dagger|0\rangle$, where both are occupied; the positively charged hole state $\hat{d}_m^\dagger|0\rangle$ (both unoccupied); and a single electron-hole pair (Frenkel excited) state $\hat{c}_m^\dagger \hat{d}_m^\dagger|0\rangle$, when HOMO electron is transferred to the LUMO. The model is shown in Fig. 1. The operators, $\hat{c}_m^\dagger$ and $\hat{d}_n^\dagger$, create an electron on site m and a hole on n, respectively ($\hat{c}_m$ and $\hat{d}_n$ are the corresponding annihilation operators). They satisfy the Fermi commutations

$$\{\hat{c}_m, \hat{c}_n^\dagger\} = \hat{c}_m \hat{c}_n^\dagger + \hat{c}_n^\dagger \hat{c}_m = \delta_{mn}, \tag{1}$$

$$\{\hat{d}_m, \hat{d}_n^\dagger\} = \hat{d}_m \hat{d}_n^\dagger + \hat{d}_n^\dagger \hat{d}_m = \delta_{mn}. \tag{2}$$

We adopt the following tight-binding Hamiltonian for electrons and holes in the monopole approximation, used in semiconductor optics. It neglects quartic electronic exchange terms,[10,11]

$$\hat{H}_S = \sum_{m,n} t_{mn}^{(1)} \hat{c}_m^\dagger \hat{c}_n + \sum_{m,n} t_{mn}^{(2)} \hat{d}_m^\dagger \hat{d}_n + \sum_{mn}^{m \neq n} W_{mn}^{(f)} \hat{c}_m^\dagger \hat{d}_m^\dagger \hat{d}_n \hat{c}_n$$

$$- \sum_{mn} W_{mn}^{(c)} \hat{c}_m^\dagger \hat{d}_n^\dagger \hat{d}_n \hat{c}_m + \frac{1}{2} \sum_{mn}^{m \neq n} V_{mn}^{(1)} \hat{c}_m^\dagger \hat{c}_n^\dagger \hat{c}_n \hat{c}_m$$

$$+ \frac{1}{2} \sum_{mn}^{m \neq n} V_{mn}^{(2)} \hat{d}_m^\dagger \hat{d}_n^\dagger \hat{d}_n \hat{d}_m. \tag{3}$$

The Hamiltonian parameters are as follows. $t_{mn}^{(1)}$ ($t_{mn}^{(2)}$) is the electron (hole) hopping rate between LUMO (HOMO) orbitals, $V_{mn}^{(1)} = V^{(e)}(|\boldsymbol{r}_m - \boldsymbol{r}_n|)$ is the electron-electron Coulomb repulsion between molecules m and n, $V_{mn}^{(2)} = V^{(h)}(|\boldsymbol{r}_m - \boldsymbol{r}_n|)$ is the hole-hole Coulomb repulsion between molecules m and n, $W_{mn}^{(f)}$ is the dipole-dipole type resonance interaction between two excitons on sites m and n, and finally $W_{mn}^{(c)} = V^{(eh)}(|\boldsymbol{r}_m - \boldsymbol{r}_n|)$ is the Coulomb attraction energy between the electron and the hole.

The system is further coupled to a harmonic phonon bath described by a Hamiltonian,

$$\hat{H}_B = \sum_\alpha w_\alpha (\hat{b}_\alpha^\dagger \hat{b}_\alpha + 1/2), \tag{4}$$

where w_α is the frequency of the phonon mode α and $\hat{b}_\alpha^\dagger$ ($\hat{b}_\alpha$) are the creation (annihilation) boson operators,

$$[\hat{b}_\alpha, \hat{b}_{\alpha'}^\dagger] = \hat{b}_\alpha \hat{b}_{\alpha'}^\dagger - \hat{b}_{\alpha'}^\dagger \hat{b}_\alpha = \delta_{\alpha\alpha'}. \tag{5}$$

The electron and hole energies fluctuate due to (linear) coupling with the bath

$$\hat{H}_{SB} = \sum_\alpha \left[\sum_m f_{\alpha,m}^{(1)} \hat{c}_m^\dagger \hat{c}_m + \sum_m f_{\alpha,m}^{(2)} \hat{d}_m^\dagger \hat{d}_m \right] (\hat{b}_\alpha^\dagger + \hat{b}_\alpha). \tag{6}$$

Here, $f_{\alpha,m}^{(1)}$ and $f_{\alpha,m}^{(2)}$ are the coupling strengths between the electron and the hole orbitals at site m and the bath coordinate. To describe the optical response, we couple the system to a classical external optical (electric) field

$$\hat{H}_{SF} = - \sum_m [\boldsymbol{\mu}_m^* \hat{d}_m \hat{c}_m + \boldsymbol{\mu}_m \hat{c}_m^\dagger \hat{d}_m^\dagger] \cdot \boldsymbol{E}(t). \tag{7}$$

This dipole interaction can only create an electron-hole pair (exciton) on the same molecule: the CT states are dark.

The total Hamiltonian is given by

$$\hat{H}_T = \hat{H}_S + \hat{H}_{SB} + \hat{H}_B + \hat{H}_{SF}. \tag{8}$$

The lowest manifold of single (one electron and one hole) excited states will be denoted by $|e_m h_n\rangle \equiv \hat{c}_m^\dagger \hat{d}_n^\dagger|0\rangle$. The Hamiltonian matrix elements for these states are

$$\langle e_m h_n | \hat{H}_S | e_k h_l \rangle = \delta_{nl} t_{mk}^{(1)} + \delta_{mk} t_{nl}^{(2)} + \delta_{kl} \delta_{mn} (1 - \delta_{mk}) W_{mk}^{(f)}$$

$$- \delta_{mk} \delta_{nl} W_{mn}^{(c)}. \tag{9}$$

This includes the state energies (diagonal part) $\langle e_m h_n | \hat{H}_S | e_m h_n \rangle = t_{mm}^{(1)} + t_{nn}^{(2)} - W_{mn}^{(c)}$ and the off-diagonal couplings. The Coulomb interaction potential is defined for charge pairs, i.e., $W_{mn}^{(c)} = e^2 (4\pi\epsilon_0 |\boldsymbol{r}_m - \boldsymbol{r}_n|)^{-1}$, when $m \neq n$. $W_{mm}^{(c)}$ is the intrinsic property of a molecule under consideration.

States where the electron and the hole reside on the same molecule, $\hat{c}_m^\dagger \hat{d}_m^\dagger |0\rangle$, represent molecular excitations. The Frenkel exciton model is thus recovered by neglecting the charged molecular states, where the electron and hole reside on different molecules. Each molecule is then a two-level system and the molecular transition energy is $\varepsilon_m = t_{mm}^{(1)} + t_{mm}^{(2)} - W_{mm}^{(c)}$ and the intermolecular interaction is $J_{mn} = W_{mn}^{(f)}$.

We next turn to the doubly-excited two electron-hole pair manifold, $|e_m e_n h_k h_l\rangle \equiv \hat{c}_m^\dagger \hat{c}_n^\dagger \hat{d}_k^\dagger \hat{d}_l^\dagger |0\rangle$. A complete basis set is obtained by using the constraints $m > n$ and $k > l$ (note that $m = n$ and $k = l$ are excluded by Pauli blocking). This gives $(N(N-1)/2)^2$ double-pair states with the following Hamiltonian matrix elements:

$$\langle e_m e_n h_k h_l | \hat{H}_S | e_{m'} e_{n'} h_{k'} h_{l'} \rangle = (t_{mm'}^{(1)} \delta_{nn'} + t_{mn'}^{(1)} \delta_{nm'} + t_{nm'}^{(1)} \delta_{mn'} + t_{nn'}^{(1)} \delta_{mm'}) \delta_{kk'} \delta_{ll'} + (t_{kk'}^{(2)} \delta_{ll'} + t_{kl'}^{(2)} \delta_{lk'} + t_{lk'}^{(2)} \delta_{kl'} + t_{ll'}^{(2)} \delta_{kk'}) \delta_{mm'} \delta_{nn'}$$

$$+ [V_{mn}^{(1)} + V_{kl}^{(2)} - W_{mk}^{(c)} - W_{ml}^{(c)} - W_{nk}^{(c)} - W_{nl}^{(c)}] \delta_{mm'} \delta_{nn'} \delta_{kk'} \delta_{ll'}$$

$$+ [W_{mm'}^{(f)} \delta_{nn'} (\delta_{mk} \delta_{ll'} + \delta_{ml} \delta_{kl'}) + W_{nm'}^{(f)} \delta_{mn'} (\delta_{nk} \delta_{ll'} + \delta_{nl} \delta_{kl'})] \delta_{m'k'}$$

$$+ [W_{mm'}^{(f)} \delta_{nn'} (\delta_{mk} \delta_{lk'} + \delta_{ml} \delta_{kk'}) + W_{nm'}^{(f)} \delta_{mn'} (\delta_{nk} \delta_{lk'} + \delta_{nl} \delta_{kk'})] \delta_{m'l'}$$

$$+ [W_{mn'}^{(f)} \delta_{nm'} (\delta_{mk} \delta_{ll'} + \delta_{ml} \delta_{kl'}) + W_{nn'}^{(f)} \delta_{mm'} (\delta_{nk} \delta_{ll'} + \delta_{nl} \delta_{kl'})] \delta_{n'k'}$$

$$+ [W_{mn'}^{(f)} \delta_{nm'} (\delta_{mk} \delta_{lk'} + \delta_{ml} \delta_{kk'}) + W_{nn'}^{(f)} \delta_{mm'} (\delta_{nk} \delta_{lk'} + \delta_{nl} \delta_{kk'})] \delta_{n'l'}. \qquad (10)$$

The singly excited,

$$|e\rangle = \sum_{mk} \psi_{mk,e} \hat{c}_m^\dagger \hat{d}_k^\dagger |0\rangle, \qquad (11)$$

and doubly excited,

$$|f\rangle = \sum_{mn}^{m>n} \sum_{kl}^{k>l} \Psi_{(mn)(kl),f} \hat{c}_m^\dagger \hat{c}_n^\dagger \hat{d}_k^\dagger \hat{d}_l^\dagger |0\rangle, \qquad (12)$$

eigenstates are calculated by diagonalizing the corresponding blocks of the Hamiltonian matrix.

III. MODELING THE ENERGY AND ELECTRON TRANSFER

All bath-induced relaxation and transport properties of our model are determined by the following matrices of spectral densities:[12]

$$C''^{(11)}_{mm,nn}(\omega) = \pi \sum_\alpha f_{\alpha,m}^{(1)} f_{\alpha,n}^{(1)} [\delta(\omega - w_\alpha) - \delta(\omega + w_\alpha)], \qquad (13)$$

$$C''^{(12)}_{mm,nn}(\omega) = \pi \sum_\alpha f_{\alpha,m}^{(1)} f_{\alpha,n}^{(2)} [\delta(\omega - w_\alpha) - \delta(\omega + w_\alpha)], \qquad (14)$$

$$C''^{(22)}_{mm,nn}(\omega) = \pi \sum_\alpha f_{\alpha,m}^{(2)} f_{\alpha,n}^{(2)} [\delta(\omega - w_\alpha) - \delta(\omega + w_\alpha)]. \qquad (15)$$

These satisfy $C''(\omega) = -C''(-\omega)$. Here, the pairs of indices denote energy (diagonal) fluctuations of the local states. For an infinite number of bath degrees of freedom, the spectral density is a smooth function.

We shall transform these matrices into the eigenstate basis, thus mapping the local correlations to correlations of fluctuations of the exciton eigenstates. The single-exciton manifold is described by a tetradic spectral density $C''_{e_4 e_3, e_2 e_1}(\omega)$. Fluctuations involving the double-exciton states have the spectral densities $C''_{e_1 e_2, f_1 f_2}(\omega)$ and $C''_{f_1 f_2, f_1' f_2'}(\omega)$. Fluctuations of eigenstate transition energies, $C''_{ee,e'e'}(\omega)$, cause pure dephasing, and the fluctuations of couplings, $C''_{ee',e'e}(\omega)$, are responsible for the energy and charge transport. The double-exciton fluctuations are responsible for the broadening of transitions involving the double-exciton states. The transformation between the real space and the eigenstate fluctuation spectral densities is given in the Appendix.

To describe exciton dephasing and transport, and the corresponding optical response in the eigenstate basis, we introduce two auxiliary bath functions. The first is the lineshape function,

$$g_{ab,cd}(t) = \int \frac{d\omega}{2\pi} \frac{C''_{ab,cd}(\omega)}{\omega^2} [\coth(\beta\omega/2)(1 - \cos(\omega t)) + i \sin(\omega t) - i\omega t], \qquad (16)$$

where the indices $abcd$ run over the manifolds g, e, and f and $\beta = (k_B T)^{-1}$. Its second derivative,

$$\ddot{g}_{ab,cd}(t) \equiv \bar{M}_{ab,cd}^{(+)}(t) = \int \frac{d\omega}{2\pi} C''_{ab,cd}(\omega) \times [\coth(\beta\omega/2)\cos(\omega t) - i \sin(\omega t)], \qquad (17)$$

is the correlation function of fluctuations.[12]

Transport in the single-exciton manifold will be described by the Pauli master equation[13]

$$\rho_{ee} = -K_{ee,ee}\rho_{ee} + \sum_{e'}^{e' \neq e} K_{ee,e'e'}\rho_{e'e'}. \tag{18}$$

The energy and charge transport rates can be calculated by including diagonal fluctuations nonperturbatively using the cumulant expansion. Off-diagonal fluctuations are treated using second order perturbation theory. The transfer rate between an initial e' and a final e state ($e \neq e'$) is obtained by assuming bath thermal equilibrium with respect to the initial state[8]

$$K_{ee,e'e'} = 2\,\mathrm{Re}\int_0^\infty d\tau F_{ee'}(\tau), \tag{19}$$

where

$$F_{ee'}(\tau) = F_{ee'}^{(0)}(\tau)[\ddot{g}_{e'e,e'e}(\tau) - (\dot{g}_{e'e,e'e'}(\tau) - \dot{g}_{e'e,ee}(\tau)$$
$$+ 2i\lambda_{e'e,e'e'})(\dot{g}_{e'e',ee}(\tau) - \dot{g}_{ee,ee'}(\tau)$$
$$+ 2i\lambda_{ee',e'e'})] \tag{20}$$

and

$$F_{ee'}^{(0)}(\tau) = \exp[-i\omega_{ee'}\tau - g_{ee,ee}(\tau) - g_{e'e',e'e'}(\tau)$$
$$+ g_{e'e',ee}(\tau) + g_{ee,e'e'}(\tau)$$
$$- 2i\tau(\lambda_{e'e',e'e'} - \lambda_{ee,e'e'})]. \tag{21}$$

Here,

$$\lambda_{ab,cd} = \int \frac{d\omega}{2\pi} \frac{C''_{ab,cd}(\omega)}{\omega} \tag{22}$$

is a reorganization-energy matrix. The diagonal elements of the rate matrix are given by $K_{ee,ee} = \Sigma_{e'}^{e' \neq e} K_{e'e',ee}$. Detailed balance ensures thermal equilibrium at long times. When the diagonal and off-diagonal fluctuations are uncorrelated, we get $K_{ee,e'e'}/K_{e'e',ee} = \exp[(\varepsilon_{e'} - \varepsilon_e - (\lambda_{e'e',e'e'} - \lambda_{ee,ee}))(k_B T)^{-1}]$.

This model uses the rotating-wave-approximation (RWA) (also known as the secular approximation) for the density matrix evolution. It has been shown that the nonsecular terms are responsible for the temperature-dependence of the absorption spectrum.[14,15] Nonsecular density matrix dynamics has been recently observed in conjugated polymers.[16] We have shown that the nonsecular terms are the source of the quantum transport.[17,18] In this paper, we invoke the RWA and focus on the overall peak pattern of CT states. Quantum electron transport can be included as was done in Ref. 18.

Equations (19)–(21) interpolate between several theories that are obtained as limiting cases. Consider weakly interacting donor (d) and acceptor (a) molecules. The system eigenstates are then direct products of the donor and acceptor states. We denote $U_{ee'} = \langle e|H_{SB}|e'\rangle$, where e and e' run over a or d states. $U_{ee'}$ is still a bath operator. Weak donor and acceptor coupling is characterized by the thermally averaged correlation function $\ddot{g}_{ad,da}(t) = \langle U_{ad}(t)U_{da}(0)\rangle$. The lineshape functions $g_{aa,aa}(t) \propto \langle U_{aa}(t)U_{aa}(0)\rangle$, $g_{dd,dd}(t) \propto \langle U_{dd}(t)U_{dd}(0)\rangle$, and $g_{aa,dd}(t) \propto \langle U_{aa}(t)U_{dd}(0)\rangle$ describe fluctuations of transition energy of acceptor, donor, and the correlation between the two, respectively. $\dot{g}_{aa,ad}(t) \propto \langle U_{aa}(t)U_{ad}(0)\rangle$ [and other similar terms in Eq. (20)] characterize the correlation between the transition energy fluctuations of the acceptor and the fluctuations of donor-acceptor coupling.

We first neglect diagonal fluctuations and assume that the off-diagonal donor-acceptor couplings are very slow (static)

$$\ddot{g}_{ad,da} = |U_{ad}|^2. \tag{23}$$

Here, $\dot{g}_{aa,ad}$, $\dot{g}_{aa,dd}$, and $\dot{g}_{aa,aa}$ vanish. Substituting this into Eqs. (19)–(22), we get

$$F_{ad}(\tau) = |U_{ad}|^2 e^{-i\omega_{ad}\tau}. \tag{24}$$

This second order perturbative rate expression implies energy conservation (Fermi's golden rule in the case of the single acceptor state)

$$K_{dd,aa}^{(G)} = K_{aa,dd}^{(G)} = 2\pi|U_{ad}|^2\delta(\omega_{ad}). \tag{25}$$

Note that the correlation function (17) depends on temperature. To include realistic bath spectral properties for off-diagonal fluctuations at finite temperature, we have to use Eq. (17) instead of Eq. (23). Neglecting diagonal fluctuations in Eq. (20), we get

$$F_{ad}(\tau) = F_{ad}^{(0)}(\tau)\ddot{g}_{ad,da}(\tau) = \ddot{g}_{ad,da}(\tau)e^{-i\omega_{ad}\tau}. \tag{26}$$

Upon substituting Eq. (17) into Eq. (26) and then into rate expression (19), we obtain the Redfield formula[19]

$$K_{aa,dd}^{(R)} = C''_{ad,da}(\omega_{ad})[\coth(\beta\omega_{ad}/2) - 1]. \tag{27}$$

The overdamped Brownian oscillator spectral density,

$$C''_{ad,da}(\omega) = 2\lambda_{ad,da}\frac{\Lambda\omega}{\omega^2 + \Lambda^2}, \tag{28}$$

is often used for describing energy transport between delocalized exciton eigenstates, weakly perturbed by environment fluctuations: Λ is the bath relaxation time and λ is the reorganization-energy matrix.[12]

Next, we consider the Förster model for energy transfer between the donor and the acceptor molecules with electrostatic interactions.[20] We assume that their transition energy fluctuations are independent. The intermolecular coupling is given by Eq. (23). The transition energy and coupling fluctuations correspond to the diagonal and off-diagonal elements of the lineshape functions in Eq. (19). In this expression, we only need the following elements: $g_{aa,aa}$, $g_{dd,dd}$, and $g_{ad,da} = g_{da,ad}$; all other combinations of indices vanish. We then have

$$F_{ad}(\tau) = F_{ad}^{(0)}(\tau)|U_{ad}|^2 \tag{29}$$

and

$$F_{ad}^{(0)}(\tau) = \exp[-i\omega_{ad}\tau - g_{aa,aa}(\tau) - g_{dd,dd}(\tau) - 2i\lambda_{dd,dd}\tau]. \tag{30}$$

Substituting these relations into Eqs. (19)–(21), we obtain the Förster rate formula:[21,22]

$$K_{ad}^{(F)} = |U_{ad}|^2 \int \frac{d\omega}{2\pi} \mathcal{A}_a(\omega)\mathcal{F}_d(\omega). \tag{31}$$

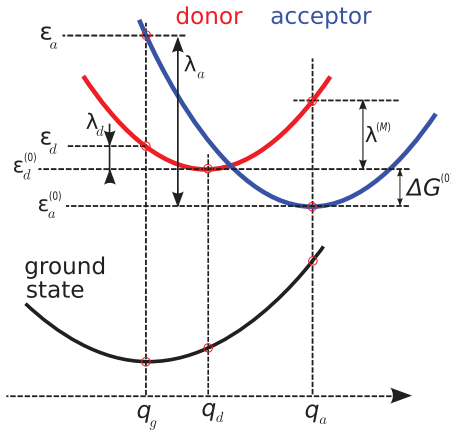FIG. 2. Ground state, donor, and acceptor state potentials along the reaction coordinate. ε_a and ε_d are defined with respect to the ground state. $\lambda_a = \varepsilon_a - \varepsilon_a^{(0)}$ and $\lambda_d = \varepsilon_d - \varepsilon_d^{(0)}$ are optical absorption reorganization energies. $\Delta G^{(0)}$ and $\lambda^{(M)}$ used in Marcus theory are defined with respect to equilibrium of the donor and the acceptor states.

Here,

$$\mathcal{A}_a(\omega) = \int d\tau \exp[i(\omega - \varepsilon_a)\tau - g_{aa,aa}(\tau)] \tag{32}$$

and

$$\mathcal{F}_d(\omega) = \int d\tau \exp[i(\omega - (\varepsilon_d - 2\lambda_{dd,dd}))\tau - g^*_{dd,dd}(\tau)] \tag{33}$$

are the acceptor absorption and donor fluorescence lineshapes, respectively, normalized to unit area. The symmetry $g(\tau) = g^*(-\tau)$ ensures that $\mathcal{A}_a(\omega)$ and $\mathcal{F}_d(\omega)$ are real. Equation (31) is commonly applied by using experimental normalized absorption and emission spectra, and the intermolecular coupling is calculated using the dipole-dipole model between transition densities.

The electron transfer theory of Marcus[23] is another special case of Eq. (19). It is obtained by assuming a single classical Gaussian bath reaction coordinate and parabolic donor and acceptor potentials for the reaction coordinate, as shown in Fig. 2. The ground, donor, and acceptor potential surfaces are $U_{gg} = wq^2/2$, $U_{dd} = \varepsilon_d^{(0)} + w(q - q_d)^2/2$, and $U_{aa} = \varepsilon_a^{(0)} + w(q - q_a)^2/2$, respectively; q is dimensionless taken to be zero at the ground state equilibrium (other quantities are defined by Fig. 2). We define the donor [$d = e'$ in Eq. (19)] reorganization energy as $\lambda_d \equiv \lambda_{e'e',e'e'} = wq_d^2/2$ and the acceptor $(a = e)$ as $\lambda_a \equiv \lambda_{ee,ee} = wq_a^2/2$. $\omega_{ad} = \varepsilon_a - \varepsilon_d$, $\varepsilon_a = \varepsilon_a^{(0)} + \lambda_a$, and $\varepsilon_d = \varepsilon_d^{(0)} + \lambda_d$ in Eq. (21) are defined with respect to the ground state equilibrium $q = 0$. These λ parameters represent optical absorption/emission reorganization energies with respect to the ground state. $\lambda_{ee,e'e'} \equiv \lambda_{aa,dd}$ and $g_{ee,e'e'} \equiv g_{aa,dd}$ characterize the correlated donor and acceptor state energy fluctuations around the equilibrium of the ground state.

Consider the fluctuations along the reaction coordinate δq in Fig. 2. The fluctuations of the ground state around the ground state equilibrium $(q \rightarrow 0)$ are $\delta U_{gg} = 0$, the donor state

fluctuations are $\delta U_{dd} = -wq_d\delta q$, and the acceptor state $\delta U_{aa} = -wq_a\delta q$. We define the correlation functions

$$\langle \delta U_{aa}(t) \delta U_{aa}(0) \rangle = w^2 q_a^2 \langle \delta q(t) \delta q(0) \rangle \tag{34}$$

and

$$\langle \delta U_{aa}(t) \delta U_{dd}(0) \rangle = w^2 q_a q_d \langle \delta q(t) \delta q(0) \rangle. \tag{35}$$

The lineshape functions and the reorganization energies are proportional to these correlation functions, and we get $g_{aa,aa}g_{dd,dd} = g^2_{aa,dd}$ and $\lambda_{aa,dd} \equiv \sqrt{\lambda_a \lambda_d}$.

The Marcus electron transfer rate is obtained by assuming Gaussian fluctuations along the reaction coordinate. This corresponds to the overdamped Brownian oscillator spectral density [Eq. (28)] in the slow fluctuation limit[24] for the diagonal fluctuations. We then get $g_{aa,aa}(t) = k_B T\lambda_a t^2$, $g_{dd,dd}(t) = k_B T\lambda_d t^2$, and $g_{aa,dd}(t) = k_B T\sqrt{\lambda_a \lambda_d} t^2$. Substituting these lineshape functions into Eq. (19), we obtain

$$F_{ad}(\tau) = F^{(0)}_{ad}(\tau)|U_{ad}|^2 \tag{36}$$

and

$$F^{(0)}_{ad}(\tau) = \exp[-i\omega_{ad}\tau - k_B T\lambda^{(M)}\tau^2 - 2i\tau(\lambda_d - \sqrt{\lambda_a \lambda_d})], \tag{37}$$

where $\lambda^{(M)} = \lambda_a + \lambda_d - 2\sqrt{\lambda_a \lambda_d}$ is a reorganization energy for the electron transfer, defined as the energy of the donor potential at the position of acceptor bath configuration along the reaction coordinate, $\lambda^{(M)} = w(q_a - q_d)^2/2$. Equation (19) now becomes a Gaussian integral that can be carried out, leading finally to the celebrated Marcus rate:

$$K^{(M)}_{ad} = 2\pi|U_{ad}|^2 \left(\frac{1}{4\pi\lambda^{(M)}k_B T} \right)^{1/2} \exp\left(-\frac{(\lambda^{(M)} - \Delta G^{(0)})^2}{4\lambda^{(M)}k_B T} \right). \tag{38}$$

Here, $\Delta G^{(0)} = \varepsilon_d - \varepsilon_a - (\lambda_d - \lambda_a)$ is the free energy difference between equilibrium positions of electron donor and acceptor potential surfaces.

The above derivation assumes positively correlated energy fluctuations of the acceptor and donor states. Such correlation is obtained when the equilibrium configuration of electron donor q_d and of acceptor q_a satisfies $q_d q_a > 0$ (the ground state potential equilibrium is at $q = 0$). In general, we have $\lambda^{(M)} = \lambda_a + \lambda_d + 2\eta\sqrt{\lambda_a \lambda_d}$, where $\eta = 1$ for positively correlated energy fluctuations of d and a and $\eta = -1$ for anticorrelated fluctuations.

IV. HAMILTONIAN PARAMETERS FOR THE REACTION CENTER OF PS-II

The single-exciton Hamiltonian and bath parameters for the PS-II reaction center have been obtained using evolutionary optimization by Novoderezhkin and Raszewski.[5–7,25,26] We used the model in Ref. 6, which includes an experimentally determined bath spectral density. We also used additional information from Refs. 5, 25, and 26.

We have simulated the energy and charge transport in the PS-II RC core consisting of six chromophores (see Fig. 3) in two branches D1 and D2. Two chlorophyll molecules, P_{D1} and P_{D2}, make the special pair. Two accessory chloro-
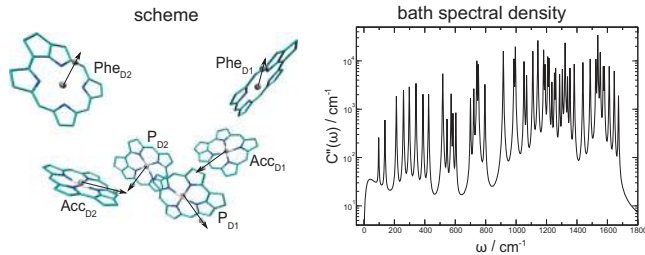
FIG. 3. Left: the RC of PS-II. Transition dipoles are represented by arrows. Right: the bath spectral density used in the simulations (Refs. 6 and 7).

phylls, Acc_{D1} and Acc_{D2}, and two pheophytins, Phe_{D1} and Phe_{D2}, are in close proximity to the special pair. We neglect two distal chlorophyll molecules considered in Ref. 6 since they interact only weakly with the core and do not perturb its excited state dynamics. Our model includes all molecular excitations of the 6 molecules. For CT states, we allow the electron to reside on any of the D1 branch molecules. The hole is allowed to reside on P_{D1}, P_{D2}, and Acc_{D1}. The CT state $Acc_{D1}^{+}P_{D1}^{-}$ is excluded since its dipole points in the opposite direction to the observed electron transfer. Altogether we thus have 12 single-exciton states (6 molecular excitations and 6 CT states). The molecular excitation energies are given by

$$\varepsilon_m \equiv \langle e_m h_m | \hat{H}_S | e_m h_m \rangle = t_{mm}^{(1)} + t_{mm}^{(2)} - W_{mm}^{(c)}. \tag{39}$$

For the electron-hole Coulomb interaction, we take

$$W_{mn}^{(c)} = \frac{k_e}{|\boldsymbol{r}_m - \boldsymbol{r}_n| + \eta}, \tag{40}$$

where $k_e = e^2(4\pi\epsilon\epsilon_0)^{-1}$ and η is a cut-off parameter, which represents screening, induced by finite charge-density distribution at short (down to zero) distances. We set $\epsilon = 1.3$ for the medium dielectric constant. For chlorophyll molecules, $\eta = 9$ Å was estimated from the length of the conjugated area of Chl and Phe.

The exciton parameters obtained in Ref. 6 determine the molecular excitation energies and the one CT state energy. We have converted them to the orbital parameters of the present model. However, the Frenkel exciton Hamiltonian does not fully specify the tight-binding model: to get the electron and hole hopping parameters and the electron and hole orbital energies, we made some additional assumptions as outlined below.

References 5, 25, and 26 give the following primary CT (radical pair) states: $RP1 = Acc_{D1}^{+}Phe_{D1}^{-}$ and $RP2 = P_{D1}^{+}Phe_{D1}^{-}$. The RP1 state energy ε_{RP1} is estimated in Ref. 6 to be inside the exciton band, while the energy of RP2 is not determined. According to Ref. 25, the free energy difference between RP1 and RP2 was estimated as 25 meV (200 cm^{-1}). We thus take $\varepsilon_{RP2} = \varepsilon_{RP1} - 200$ cm^{-1}. This information becomes sufficient to determine all diagonal parameters for the D1 branch. We denote the following Coulomb interaction energies: $W^{(0)} = k_e \eta^{-1}$ is the CT pair stabilization energy (Coulomb energy within a molecule), $W_{RP2}^{(c)} = k_e(|\boldsymbol{R}_{P_{D1}} - \boldsymbol{R}_{Phe_{D1}}| + \eta)^{-1}$ and $W_{RP1}^{(c)} = k_e(|\boldsymbol{R}_{Phe_{D1}} - \boldsymbol{R}_{Acc_{D1}}| + \eta)^{-1}$, where $\boldsymbol{R}_{Phe_{D1}}$ is the mass center of N atoms of Phe_{D1} molecule and the same is

assumed for other molecules central coordinates. These are Coulomb energies between P_{D1} and Phe_{D1}, and Phe_{D1} and Acc_{D1}, respectively. From Eq. (39), we have

$$\varepsilon_{RP1} = t_{Phe_{D1},Phe_{D1}}^{(1)} + t_{Acc_{D1},Acc_{D1}}^{(2)} - W_{RP1}^{(c)}, \tag{41}$$

$$\varepsilon_{RP2} = t_{Phe_{D1},Phe_{D1}}^{(1)} + t_{P_{D1},P_{D1}}^{(2)} - W_{RP2}^{(c)}. \tag{42}$$

We can now relate the hole energies $t_{Acc_{D1},Acc_{D1}}^{(2)}$ and $t_{P_{D1},P_{D1}}^{(2)}$ to $t_{Phe_{D1},Phe_{D1}}^{(1)}$. Using excitation transition energies of D1 branch molecules P, Acc, Phe, and value of $W^{(0)}$, we get all electron and hole level energies of the D1 branch as a function of $t_{Phe_{D1},Phe_{D1}}^{(1)}$. This parameter provides an absolute energy reference point, all optical properties are given in terms of electron-hole pairs. The D2 branch energies are taken to be the same as D1. The hole energies are obtained from the molecular exciton energies.

The off-diagonal elements t_{mn} define the electron and hole hopping energies, which determine the couplings between neutral excitations (denoted by Acc_{D1}^{*}) and CT states. In Ref. 6, the coupling of RP1 to an exciton state is assumed to be 35 cm^{-1}. We let the electrons and holes hop between all available states. The electron and hole orbital wave functions vary exponentially with distance,

$$t_{mn}^{(1)} = t_{mn}^{(2)} = A \exp(-|\boldsymbol{r}_m - \boldsymbol{r}_n|/\rho). \tag{43}$$

We assumed $A = 350$ cm^{-1} and $\rho = 4.5$ Å, which is half the molecular size η, gives Acc_{D1}^{*} and RP1 coupling of 34 cm^{-1}. The resulting single-exciton Hamiltonian is given in Table I.

To determine the system-bath coupling, we start with the model of Ref. 28, which assumes that each molecular excitation (and CT states) is coupled to its own independent bath, consisting of 48 high-frequency underdamped modes and a single overdamped low-frequency mode. We extend it to our tight-binding Hamiltonian as follows. We assume that the electron and hole levels of different molecules fluctuate independently. The spectral densities can then be written as $C''^{(11)}_{mm,nn}(\omega) = \delta_{mn} d^{(11)} \mathcal{C}(\omega)$, $C''^{(12)}_{mm,nn}(\omega) = \delta_{mn} d^{(12)} \mathcal{C}(\omega)$, and $C''^{(22)}_{mm,nn}(\omega) = \delta_{mn} d^{(22)} \mathcal{C}(\omega)$, where $\mathcal{C}(\omega)$ is given by Eq. (D2) of Ref. 28 and is shown in Fig. 3. By taking $d^{(11)} = d^{(22)} = 0.8$ and $d^{(12)} = -0.3$, we find that all molecular excitation transition energies fluctuate according to $\mathcal{C}(\omega)$ and all CT states have a spectral density $1.6\mathcal{C}(\omega)$.[6]

Equation (10) defines the double-exciton states and their fluctuation properties are given by Eqs. (A2) and (A3). The double-exciton basis set is constructed out of the allowed electron-hole configurations taking into account that each orbital can only accommodate one electron (Pauli blocking). This yields the 41 double-exciton states listed in the supplementary material.[29]

The single- and the double-exciton eigenstates were obtained by numerical diagonalization of the corresponding Hamiltonian blocks, and the spectral densities were transformed to the eigenstate basis. The exciton transport and charge transfer rates for single-exciton eigenstates were calculated using Eqs. (19)–(22).

TABLE I. Single-exciton Hamiltonian in (cm^{-1}) calculated using 2.9 resolution structure parameters (Ref. 3) [Protein Data Bank (PDB) database file 3BZ1.pdb]. The intermolecular $W_{mn}^{(f)}$ dipole-dipole interactions were computed using transition dipole directions taken from Ref. 27 and transition amplitudes $|\boldsymbol{\mu}_{\text{Chl}}|=4.4$D and $|\boldsymbol{\mu}_{\text{Phe}}|=3.4$D.

	P_1^*	$P_1^-P_2^+$	P_2^*	$Acc_1^-P_1^+$	$Acc_1^-P_2^+$	Acc_1^*	Acc_2^*	$Phe_1^-P_1^+$	$Phe_1^-P_2^+$	$Phe_1^-Acc_1^+$	Phe_1^*	Phe_2^*
P_1^*	15 190											
$P_1^-P_2^+$	63.7	19 744.7										
P_2^*	160	63.7	15 180									
$Acc_1^-P_1^+$	37.8	0	0	19 083.3								
$Acc_1^-P_2^+$	0	37.8	23.7	63.7	19 543.2							
Acc_1^*	4.78	0	−39.6	37.8	23.7	15 000						
Acc_2^*	−50.4	0	17.9	0	0	15	15 130					
$Phe_1^-P_1^+$	11.1	0	0	34	0	0	0	14 920				
$Phe_1^-P_2^+$	0	11.1	6.46	0	34	0	0	63.7	15 237.3			
$Phe_1^-Acc_1^+$	0	0	0	0	0	34	0	37.8	23.7	15 120		
Phe_1^*	−3.02	0	5.42	0	0	65.9	−3.09	11	6.46	34	15 050	
Phe_2^*	4.39	0	−5.67	0	0	−2.86	60.9	0	0	0	0.65	15 060

V. OPTICAL 2D SIGNALS WITH INHOMOGENEOUS BROADENING

2D optical signals represent the response of the system to three ultrashort chronologically ordered laser pulses with wavevectors k_1, k_2, and k_3: k_1 comes first, followed by k_2, and then k_3. The third order signals are generated in the $\pm k_1 \pm k_2 \pm k_3$ directions. The three time intervals between pulses, t_1, t_2, and t_3, serve as the control parameters. Various contributions to the third order response function may be observed by signals in different directions. We first consider the photon echo $k_I = -k_1 + k_2 + k_3$. The 2D spectrum is obtained by performing two-dimensional Fourier transform with respect to the first and third intervals ($t_1 \to \Omega_1$ and $t_3 \to \Omega_3$; all time delays between pulses are positive) and the second time interval, t_2, is varied as a parameter. This *rephasing* 2D signal shows correlations of single excitons between absorbed, Ω_1, and emitted, Ω_3, energies, exciton transport takes place during t_2. A different *nonrephasing* signal is obtained along $k_{II} = k_1 - k_2 + k_3$ (in experiment the signal direction is kept the same as in k_I, but pulses 1 and 2 are interchanged). The 2D signal is again obtained by the Fourier transform $t_1 \to \Omega_1$ and $t_3 \to \Omega_3$, respectively. Finally, we consider the *double-quantum coherence* signal in the direction $k_{III} = k_1 + k_2 - k_3$. Here, the Fourier transform can be made in two ways: either $t_1 \to \Omega_1$, $t_2 \to \Omega_2$, holding t_3 as a parameter, or $t_2 \to \Omega_2$, $t_3 \to \Omega_3$, holding t_1 as a parameter. In this signal the Ω_2 axis shows double-exciton resonances and their distribution between single excitons on Ω_1 or Ω_3 axes.[30] These signals have been described in Ref. 12.

The 2D signals were calculated by summing over various system-field interaction configurations (Liouville space pathways) in the eigenstate basis.[12,31] Equations (141)–(153), (166), and (179) of Ref. 12 were used to calculate the time domain third order response functions and Eq. (13) for the time domain linear response function. We assume Gaussian pulses with 14 500 cm^{-1} central frequency and 20 fs full width at half maximum (fwhm). The pulse envelopes, $\mathbb{E}(\omega)$, were included in the 2D signals[32] by extending Eq. (42) of Ref. 12. The absorption spectrum was calculated using Eq. (268) of Ref. 12. The signals calculated this way will be denoted homogeneous: $S_{k_I}^{(\text{hom})}$, $S_{k_{II}}^{(\text{hom})}$, and $S_{k_{III}}^{(\text{hom})}$ for the 2D

signals and $\kappa_A^{(\text{hom})}$ for the absorption. Uncorrelated diagonal disorder in transition energies was included in Ref. 6 to simulate inhomogeneous broadening (static fluctuations). This involves numerical statistical averaging of the final signal over the fluctuations. However, the protein-induced electrostatic fields should have long correlation distance, longer than the intermolecular distances in the RC core. In that case the molecular transition energies are more likely to experience correlated fluctuations. For Gaussian statistics, such fluctuations can be accounted for by a cumulant expansion technique with a line-broadening function $g(t) = \sigma_e^2 t^2 / 2$; here, σ_e denotes the variance of fluctuations. For fully correlated fluctuations of molecular transition energies, we get in the eigenstate basis for all single excitons,

$$g_{ee,e'e'}^{(\text{inh})}(t) = \tfrac{1}{2}\sigma_e^2 t^2. \qquad (44)$$

For the double-exciton transitions, we then similarly get $g_{ee,ff}^{(\text{inh})} = 2g_{ee,e'e'}^{(\text{inh})}(t)$ and $g_{ff,f'f'}^{(\text{inh})} = 4g_{ee,e'e'}^{(\text{inh})}(t)$. The total third order 2D time domain signal including inhomogeneous broadening is finally given by

$$S_{k_I}(t_3,t_2,t_1) = S_{k_I}^{(\text{hom})}(t_3,t_2,t_1)\exp\left(-\frac{\sigma_e^2}{2}(t_1-t_3)^2\right), \qquad (45)$$

$$S_{k_{II}}(t_3,t_2,t_1) = S_{k_{II}}^{(\text{hom})}(t_3,t_2,t_1)\exp\left(-\frac{\sigma_e^2}{2}(t_1+t_3)^2\right), \qquad (46)$$

$$S_{k_{III}}(t_3,t_2,t_1) = S_{k_{III}}^{(\text{hom})}(t_3,t_2,t_1)\exp\left(-\frac{\sigma_e^2}{2}(t_1+2t_2+t_3)^2\right). \qquad (47)$$

Numerical Fourier transforms were performed on the time domain signals to get 2D spectra as described above. The absorption spectrum is given by

$$\kappa_A(\omega) = \frac{1}{\sqrt{2\pi}\sigma_e}\int d\omega_1 \kappa_A^{(\text{hom})}(\omega_1)\exp\left(-\frac{(\omega_1-\omega)^2}{2\sigma_e^2}\right). \qquad (48)$$

We used $\sigma_e = 51$ cm^{-1}, which gives inhomogeneous absorption linewidth of 80 cm^{-1} fwhm.[6] This approach consider-
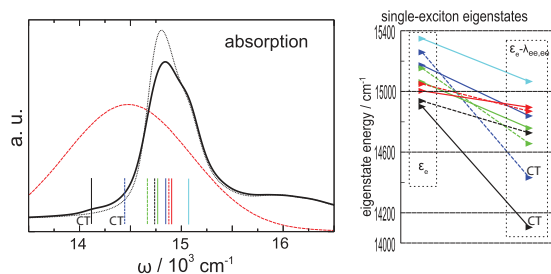
FIG. 4. Left: simulated absorption spectra of PS-II RC core at 77 K. Solid black—full model; dotted black—model without CT states. Red curve—square root of pulse power spectrum $\mathbb{E}(\omega)$ used in nonlinear optical signal simulations. Vertical lines denote positions of single excitons after reorganization. Contributions of CT states to these eigenstates (from left to right) are 0.94, 0.98, 0.63, 0.07, 0.35, 0, 0.03, 0, and 0. Right: the single-exciton eigenstates below 18 000 cm^{-1} and their reorganization shifts; three additional dark CT states at ~19 000 cm^{-1} are not shown. Exciton eigenenergies, ε_e, and reorganization-energy shifts, $\varepsilon_e - \lambda_{ee,ee}$, are shown.

ably reduces the computational cost since explicit averaging over fluctuations is not necessary.

VI. SPECTROSCOPY OF THE CT STATES

All calculations were performed at 77 K. The simulated absorption spectrum of the PS-II RC shown in Fig. 4 has a strong peak at ~15 000 cm^{-1} and a higher-energy wing at 16 000 cm^{-1} caused by underdamped bath modes. The main exciton band has a higher-energy shoulder reflecting a double-peak structure of the dimeric RC special pair. It is important to note that the bath significantly shifts the absorption peaks with respect to the vertical transitions, $\omega_{eg} = \varepsilon_e$. The absorption reorganization energies are ~200 cm^{-1}. The calculated reorganization energies for all exciton states [Eq. (22)] are shown in Fig. 4 as well. Few eigenstates have very large reorganization energies. These are mostly localized on the CT states. The eigenstates with smallest reorganization energies are mostly Frenkel excitons. The stick spectrum, embedded in the figure, shows the reorganized energies, $\varepsilon_e - \lambda_{ee,ee}$. The shoulders at 14 100 and 14 400 cm^{-1} are mostly CT states, while the strongest peak is made of several overlapping exciton bands. The spectra of PS-II RC calculated using the Frenkel exciton model by neglecting the CT states show that CT states affect the area below 15 000 cm^{-1}. They amplify the peak at ~14 800 cm^{-1} and are responsible for the 14 100 and 14 400 cm^{-1} shoulders. Indeed, the peaks at 14 100 and 14 400 cm^{-1} are absent for the Frenkel exciton model.

Figure 5 shows the simulated exciton population and charge transfer dynamics according to Pauli master equation between 10 fs and 1 ps calculated using the rates of Eq. (19). The figure reveals tightly coupled dynamics in the RC core: all populations redistribute within 10–500 fs. This leads to thermal equilibrium where the population accumulates in a CT state (state 6). The final thermal equilibrium does not exactly match the Boltzmann distribution for the reorganized energies $\varepsilon_e - \lambda_{ee,ee}$ since we include correlations between the diagonal and the off-diagonal fluctuations via functions $\dot{g}_{ee,ee'}$, which affect the transport rates. A comparison with the Frenkel exciton model, where CT states are excluded (Fig. 5), shows that CT states do not strongly alter the energy
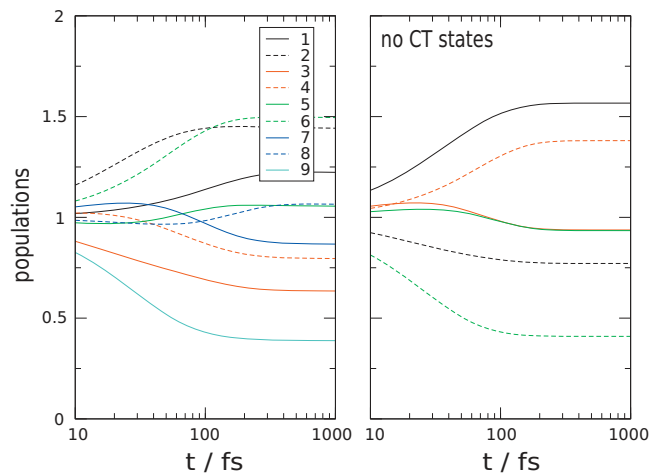

FIG. 5. Exciton population dynamics when all states are initially equally populated, $\rho_{ee} = 1$ (the three high-energy, ~19 000 cm^{-1} CT states are not shown). The states are numbered by their energy ε_e; color code is the same as in Fig. 4.

relaxation time scale in the core RC. The entire complex, including CT and Frenkel excitons, participates in the charge separation.

We next present the 2D signals for the pulse polarization configuration $xxyy$: $\boldsymbol{k}_1$ and $\boldsymbol{k}_2$ are y polarized, $\boldsymbol{k}_3$ and the detector have x polarization. This is one of the three primary tensor components yielding the orientationally averaged signal for an isotropic solution. The amplitude of the single interaction configuration is

$$\langle (\boldsymbol{\mu}_4 \cdot \boldsymbol{x})(\boldsymbol{\mu}_3 \cdot \boldsymbol{x})(\boldsymbol{\mu}_2 \cdot \boldsymbol{y})(\boldsymbol{\mu}_1 \cdot \boldsymbol{y}) \rangle$$
$$= 4(\boldsymbol{\mu}_4 \cdot \boldsymbol{\mu}_3)(\boldsymbol{\mu}_2 \cdot \boldsymbol{\mu}_1) - (\boldsymbol{\mu}_4 \cdot \boldsymbol{\mu}_2)(\boldsymbol{\mu}_3 \cdot \boldsymbol{\mu}_1)$$
$$- (\boldsymbol{\mu}_4 \cdot \boldsymbol{\mu}_1)(\boldsymbol{\mu}_3 \cdot \boldsymbol{\mu}_2). \tag{49}$$

We define the signal as the normalized imaginary (absorptive) parts of the calculated inhomogeneous signals,

$$\mathbb{S} = 10 \, \mathrm{Im}(S)/S^{(N)}, \tag{50}$$

where $S^{(N)}$ is a real normalization constant. All 2D spectra are then plotted using the nonlinear scale,

$$\mathrm{arcsinh}(\mathbb{S}) = \ln(\mathbb{S} + \sqrt{1 + \mathbb{S}^2}) \tag{51}$$

which reveals both strong and weak features: for $|\mathbb{S}| < 1$, $\mathrm{arcsinh}(\mathbb{S}) \approx \mathbb{S}$ and $\mathrm{arcsinh}(\mathbb{S}) \approx (\mathbb{S}|\mathbb{S}|^{-1})\ln(2|\mathbb{S}|)$ otherwise. The color code is shown in the figures.

The 2D $\boldsymbol{k}_I$ spectra are shown in Fig. 6. The main exciton resonances appear at 14 500–15 500 cm^{-1}, resembling the absorption. Peaks are elongated along the diagonal due to inhomogeneous broadening. At zero delay, blue diagonal peaks denote the fundamental exciton transitions. Only one diagonal peak can be clearly resolved. The 14 100 cm^{-1} peak represents the primary CT state since it is not present in the corresponding simulations without CT states (middle column). The broad high-energy ~16 000 cm^{-1} wing does not appear on the diagonal of the 2D spectrum, but it is mapped on the off-diagonal cross-peak regions along Ω_1 and Ω_3.

In the right column of Fig. 6 we display the corresponding 2D difference spectrum of the full model and the Frenkel exciton model normalized to its maximum. CT states
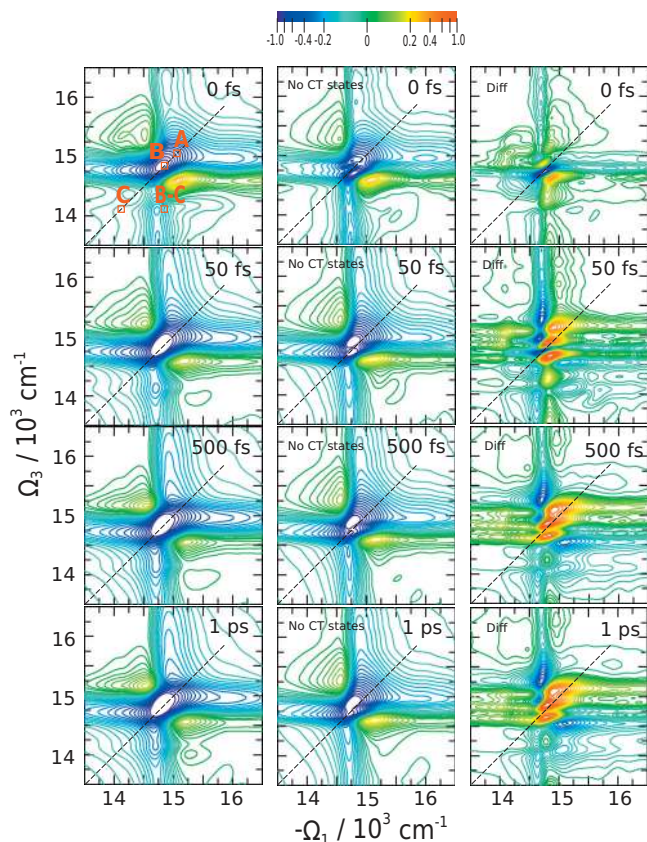
FIG. 6. 2D photon echo (rephasing) signal. Left—full model, middle—Frenkel model (no CT states), and right—the difference. Each plot is scaled according to Eq. (51) and normalized [Eq. (50)] as follows: for left and middle columns, $S^{(N)}$ is the maximum at zero delay time; for the right column, $S^{(N)}$ is the maximum of each signal.

strongly influence the exciton band as seen at 0 fs delay. At later times, the different relaxation results in a vertical peak distribution. The positive peaks at the diagonal around 15 000 cm^{-1} show that in the Frenkel model the energy remains in this area at long time. In the full model, the energy is transferred to lower-lying CT states below the diagonal ($\Omega_3 \approx 14\ 000$ cm^{-1}).

We mark three regions on the diagonal (A–C) and one cross-peak region (B-C). These correspond to the two exciton bands and the CT state. In Fig. 7 we show the time evolution of these regions. The diagonal regions grow stronger. Peaks A and B change most strongly on an absolute scale. However, the relative change of these areas with respect to their initial amplitudes is different: A changes by 30%, B changes by 24% and C changes by 146%. All peaks do grow and the internal redistribution of energy between the regions is as follows: A and B (Frenkel exciton bands) decay into C (CT exciton). The absolute peak growth is related to the pulse-envelope since the pulse is centered at 14 500 cm^{-1}. The CT peak C is poorly resolved on the diagonal, similar to the absorption. The dynamics in the B-C cross-peak region is a significantly new feature not available from linear optical techniques, which reveals the charge-separation process.

To trace the origin of the 2D peaks, in Fig. 8 we plot separately the three contributions: ground state bleaching (GSB), excited state emission (ESE), and excited state ab-
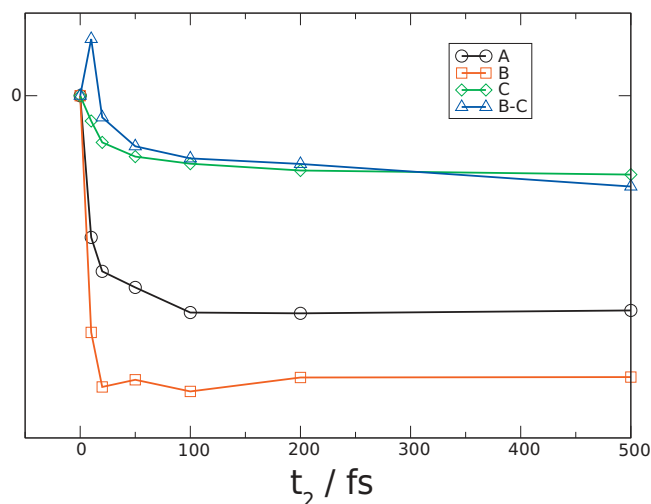

FIG. 7. Time dependence of integrated amplitudes in regions A–C and their cross-peaks (marked by squares in Fig. 6). The traces are shifted vertically to make the initial amplitude 0.

sorption (ESA). The corresponding Feynman diagrams are shown on the right. ESE is much weaker than the GSB or ESA. This is because the absorption and emission frequencies are different due to the Stokes shift induced by under-
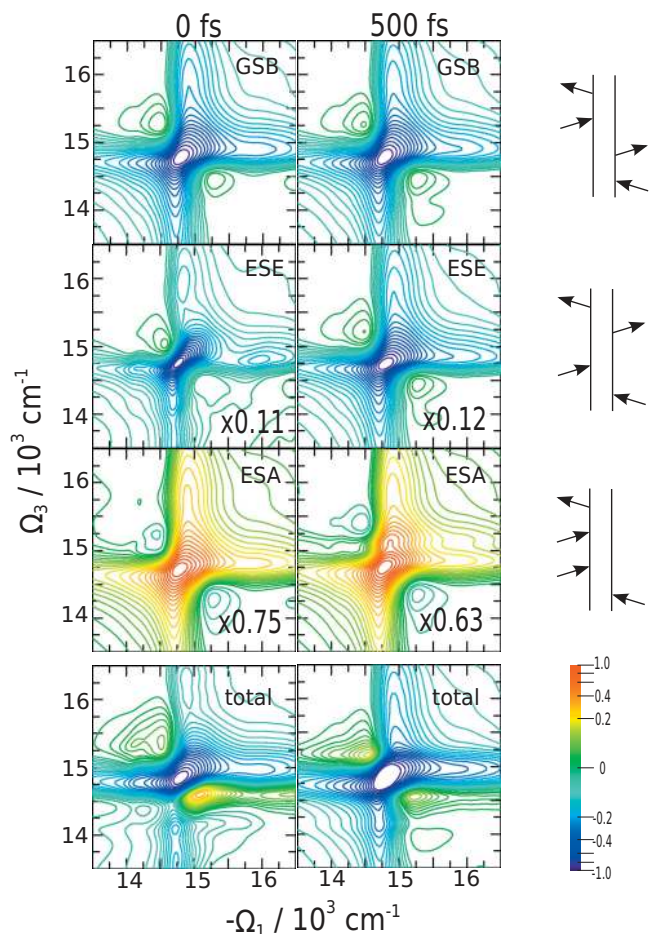

FIG. 8. The three components contributing to the 2D k_{I} spectra at two t_2 delay times. The amplitudes of the ESE and ESA components have been multiplied by the factors given in each panel. The signal is scaled according to Eq. (51) and $S^{(N)}$ [Eq. (50)] is the maximum of each plot.
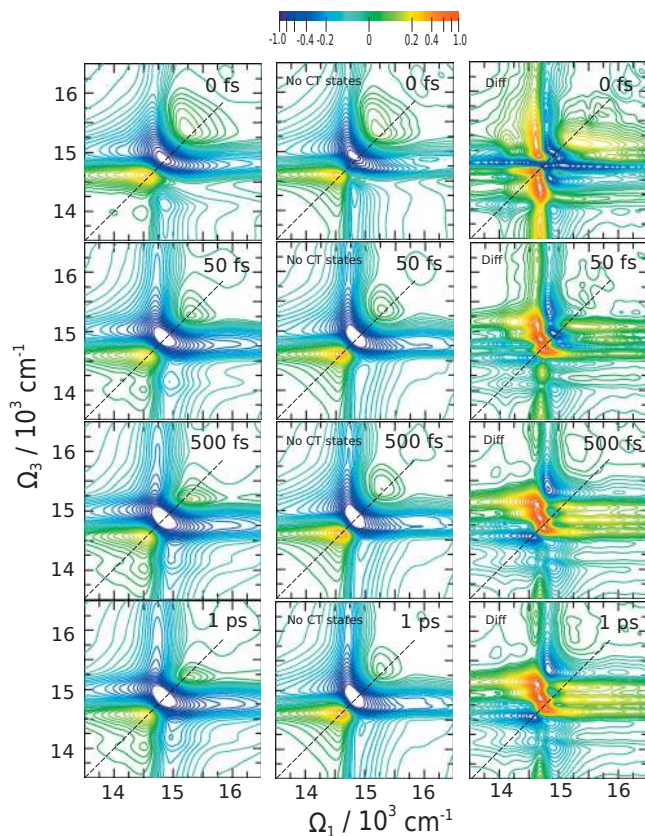
FIG. 9. 2D photon echo (nonrephasing) signal k_{II}. Left—full model, middle—Frenkel model (no CT states), and right—the difference. The signal is scaled according to Eq. (51) and normalized [Eq. (50)] as follows: for left and middle columns, $S^{(N)}$ is the maximum at zero delay time; for the right column, $S^{(N)}$ is the maximum of the signal of each plot.
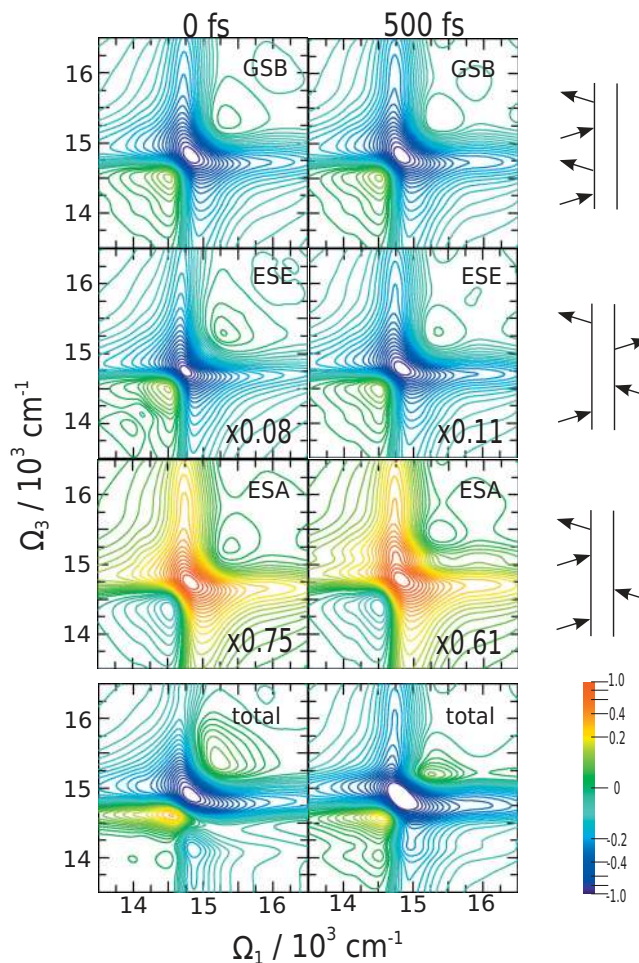

FIG. 10. The three components contributing to the 2D k_{II} spectra at two t_2 delay times. The numbers inside the plots are the relative amplitudes of the component, compared to GSB. Each plot is scaled according to Eq. (51) and normalized [$S^{(N)}$ in Eq. (50)] to the maximum.

damped bath modes. Since our optical pulses are centered at the single exciton frequencies, they select mostly GSB and ESE. GSB weakly depends on the t_2 delay time. ESE shows t_2 dependent broadening of the main exciton band and Frenkel exciton population decay into CT state reflected in the cross-peak B-C region. ESA has an opposite sign than ESE and GSB and a different time evolution. It shows buildup of the cross-peak region above the diagonal. The ESE, GSB, and ESA overlap and the total signal shows strong interference.

The excited state absorption (yellow-red peaks) below the diagonal in the total signal contains remarkably strong features. These are different from our previous simulations on the Fenna–Mathews–Olson complex[33,34] and the PS-I photosystem.[35] We find very strong positive peaks below the diagonal line with or without the CT states. This ESA feature is related to the underdamped bath modes, which were not included in our earlier simulations. The bath induces large reorganization energies. Thus, the absorption and the fluorescence frequencies are shifted. This shows up in the difference between the ground state absorption and the excited state absorption frequencies.

The k_{II} (nonrephasing) signal is displayed in Fig. 9. Its lineshapes are oriented antidiagonally. Otherwise, the k_{II} spectrum features are similar to k_I. However, the ESA creates a strong positive diagonal peak at 14 700 cm^{-1}. This peak survives in the Frenkel exciton model with no CT states as

the excitons relax during t_2. In the CT state model, that peak slowly decreases with t_2 as the CT states are populated. The difference spectrum of the k_{II} signal (right column) shows a complex pattern resulting from extensive overlaps of the positive and negative features. The strongest features are at $|\Omega_1| < 15\,000$ cm^{-1}. Positive and negative features arise when CT states are depleted or added to the intensity of the signal. The peaks around $\Omega_3 \approx 14\,000$ cm^{-1} are clear features of the CT states and trace the charge separation process.

In Fig. 10 we show the GSB, ESE, and ESA contributions to the total k_{II} signal and their Feynman diagrams. Again, the ESE contribution is relatively weak due to the finite pulse bandwidth. The t_2 dynamics in different components is not that well resolved as in k_I since all lineshapes are much broader. The total signal thus reflects strong interference between these various contributions. However, the interference filters out most of the static features and the B-C cross-peak region shows buildup of amplitude with t_2 even more clearly than in the k_I signal.

The double-exciton dynamics is monitored by the double-quantum coherence (2QC) signals (k_{III}). Figure 11 shows two types of 2QC signals. Four-to-six double-exciton-related peaks are clearly seen. As shown earlier, double-exciton peaks, which are delocalized between single-exciton
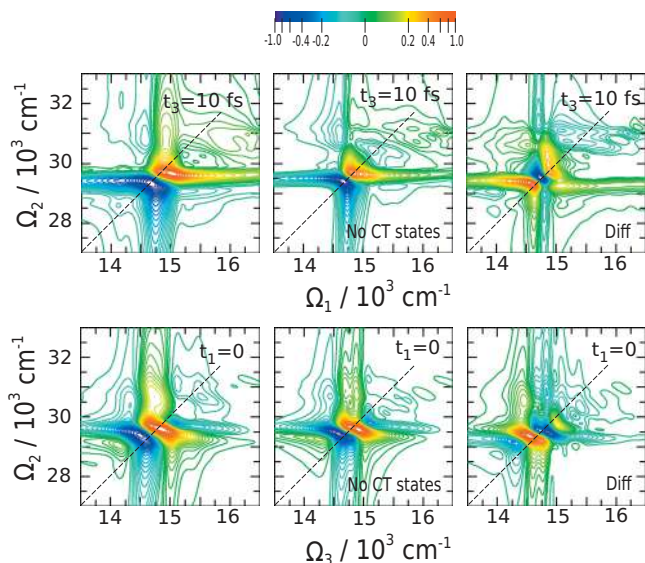
FIG. 11. 2D double-quantum-coherence signals. Left—full model, middle—Frenkel exciton model (no CT states), and right—the difference. Each plot is scaled according to Eq. (51) and normalized [$S^{(N)}$ in Eq. (50)] to the maximum.

FIG. 12. The two pathways of the k_{III} signals and their corresponding Feynman diagrams. Each plot is scaled according to Eq. (51) and normalized [$S^{(N)}$ in Eq. (50)] to the maximum.

product states dominate the 2D spectra[30] since the underlying system is made of two-level molecules. The CT states do not change this picture since they have no transition dipole moment. The strongest peaks lie within the main exciton band close to the dashed line, which marks $\Omega_2 = 2\Omega_1$ or $\Omega_2 = 2\Omega_3$. CT states again show up in the Ω_1, Ω_2 plot as additional peaks especially at $\Omega_1 = 14\,100$ cm^{-1}. Signatures of CT states in the Ω_2, Ω_3 plot are less visible. The difference spectrum shows the sensitivity of the spectrum to the CT states and helps determine the specific peaks related to the CT states: they span the whole exciton band and may not be isolated opposite from k_I and k_{II}.

In Fig. 12 we display the two pathways contributing to the 2D peaks in k_{III} and their Feynman diagrams. Again, the total signal contains positive and negative contributions with extensive overlap. The most prominent peaks show up in the main Frenkel exciton area ($\Omega_1 = 14\,500 - 15\,000$ cm^{-1}), indicating that double excitons in this region are highly delocalized between the Frenkel excitons and the CT states.

VII. SUMMARY AND DISCUSSION

In this paper, we have simulated three third order two-dimensional spectra of the PS-II RC core complex. These cover all possible exciton density matrix evolution pathways, induced by three weak laser pulses. The simulated 2D signals show clear signatures of charge transfer. These are usually weak in absorption since CT eigenstates only borrow oscillator strength from molecular excitations. However, the cross-peaks are amplified in the 2D spectra by other strong diagonal peaks, making CT transitions easy to resolve. The CT cross-peak amplitudes allow one to monitor the charge-separation process and its time scale, and may help identify the primary CT state configuration when comparing to experiments. The double-quantum-coherence signal contains a
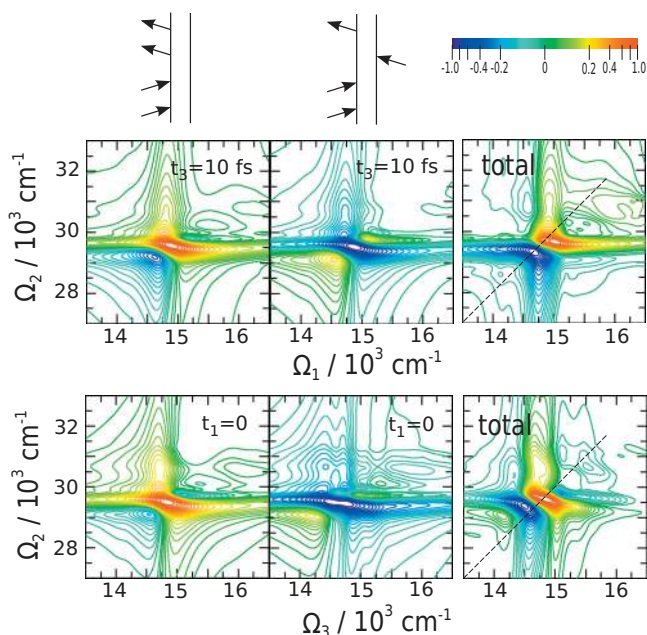
complex pattern of interfering contributions. It shows strong couplings inside the core of RC of the PS-II through delocalization of double-exciton eigenstates.

Several novel theoretical developments were used in the simulations. First, we have incorporated charge transfer states into the molecular complex model. Frenkel excitons, CT states, their couplings, and the double-exciton manifold are defined microscopically. The tight-binding model requires more information about the system than contained in the Frenkel exciton model. These parameters include molecular HOMO and LUMO wave functions and the corresponding charge distributions. These may be readily obtained from *ab initio* simulations. Here, we compiled the parameter set using previous model simulations.

The second important feature is the interplay of under-damped and overdamped bath modes. This has been used previously in the modeling of linear optical signals and transport rates. The effect of one underdamped vibrational mode of a two-level electronic system in 2D spectroscopy has been analyzed.[36] However, how the underdamped bath vibrations affect the 2D optical signals of an excitonic aggregate is an open question. We find that absorption bands coming from vibrational high-energy transitions affect the off-diagonal (cross-peak) regions and do not appear on the diagonal. This is interesting since it allows one to determine the origin of optical absorption transitions: electronic transitions appear on the diagonal in the 2D spectra, while additional vibrational bands appear on the off-diagonal region.

Previous studies accounted for the inhomogeneous broadening by using uncorrelated diagonal disorder. This approach is very well suited for extended molecular aggregates in solutions. The protein environment is the main cause of static inhomogeneities in photosynthetic aggregates. However, since proteins extend over distances longer than the distances within pigment molecules in the RC core, all inho-

mogeneities are expected to show some degree of correlation. Here, we assumed completely correlated fluctuations, where static energy shifts of all molecules are identical. Energy gaps between different excitons in the same band are not affected by such shifts. This model therefore does not affect intraband exciton dephasing and transport rates.

The applicability of uncorrelated vs. correlated disorder models depends on the system under consideration. For small compact aggregates embedded in large proteins, the correlated disorder model may be applicable. For a large bulk system, we expect the uncorrelated disorder model to hold. However, more advanced models should define the correlation distance so that the degree of correlation depends on how far are the molecules from each other, as was done in Refs. 37 and 38. Determining the correlation distance in excitonic aggregates is an interesting topic for future studies.

In the case of fully correlated Gaussian diagonal disorder, the compact time-domain expressions [Eqs. (45)–(47)] apply. This approach avoids the explicit ensemble averagings. Our simulated features in 2D signals show typical diagonally elongated peak shapes, which signify inhomogeneous broadening. The spectral dynamics with the third, t_2, axis is not affected by the correlated disorder.

It is important to note that a homogeneous peak may show elongations in 2D plots as well. This happens since the shape of an absorptive part of the peak, made of two Lorentzians (one along one axis and the other along the other axis), has single sign in one diagonal direction and it shows two sign flips across that diagonal. However, the absolute value signal (Re^2+Im^2) has a symmetric crosslike feature, which

has no elongation along the diagonal. Inhomogeneities induce additional diagonal elongation, which is larger than the elongation of the homogeneous signal, when the inhomogeneous broadening is large. Our simulations (not shown) reveal that the inhomogeneities-induced elongation shows up even in the absolute value plot.

ACKNOWLEDGMENTS

APPENDIX: TRANSFORMATION OF THE SPECTRAL DENSITIES

Here, we provide expressions that transform the spectral densities defined in Eqs. (13)–(15) into the eigenstates basis and connect local energy correlations to correlations of the fluctuations of exciton eigenstates.

For the single-exciton manifold, we have

$$C''_{e_4 e_3, e_2 e_1}(\omega) = \sum_{mn}\sum_{kl} \psi^*_{mn,e_4}\psi_{mn,e_3}\psi^*_{kl,e_2}\psi_{kl,e_1}$$
$$\times [C''^{(11)}_{mm,kk}(\omega) + C''^{(12)}_{mm,ll}(\omega)$$
$$+ C''^{(12)}_{kk,nn}(\omega) + C''^{(22)}_{nn,ll}(\omega)]. \quad (A1)$$

Fluctuations of the eigenstate transition energies, $C''_{ee,e'e'}(\omega)$, cause pure dephasing, and the induced fluctuations of couplings, $C''_{ee',e'e}(\omega)$, are responsible for energy and charge transport. The correlated single and double-exciton fluctuations are

$$C''_{e_1 e_2, f_1 f_2}(\omega) = \sum_{m_1 n_1}\sum_{m_2 n_2}^{m_2>n_2}\sum_{k_2 l_2}^{k_2>l_2} \psi^*_{m_1 n_1,e_1}\psi_{m_1 n_1,e_2}\Psi^*_{(m_2 n_2)(k_2 l_2),f_1}\Psi_{(m_2 n_2)(k_2 l_2),f_2}[C''^{(11)}_{m_1 m_1,m_2 m_2}(\omega) + C''^{(12)}_{m_1 m_1,n_2 n_2}(\omega)$$
$$+ C''^{(11)}_{m_1 m_1,k_2 k_2}(\omega) + C''^{(12)}_{m_1 m_1,l_2 l_2}(\omega) + C''^{(12)}_{m_2 m_2,n_1 n_1}(\omega) + C''^{(22)}_{n_1 n_1,n_2 n_2}(\omega) + C''^{(12)}_{k_2 k_2,n_1 n_1}(\omega)$$
$$+ C''^{(22)}_{n_1 n_1,l_2 l_2}(\omega)]. \quad (A2)$$

Finally, the double-exciton fluctuations are given by

$$C''_{f_4 f_3, f_2 f_1}(\omega) = \sum_{m_1 n_1}^{m_1>n_1}\sum_{k_1 l_1}^{k_1>l_1}\sum_{m_2 n_2}^{m_2>n_2}\sum_{k_2 l_2}^{k_2>l_2} \Psi^*_{(m_1 n_1)(k_1 l_1),f_4}\Psi_{(m_1 n_1)(k_1 l_1),f_3}\Psi^*_{(m_2 n_2)(k_2 l_2),f_2}\Psi_{(m_2 n_2)(k_2 l_2),f_1}[C''^{(11)}_{m_1 m_1,m_2 m_2}(\omega)$$
$$+ C''^{(12)}_{m_1 m_1,n_2 n_2}(\omega) + C''^{(11)}_{m_1 m_1,k_2 k_2}(\omega) + C''^{(12)}_{m_1 m_1,l_2 l_2}(\omega) + C''^{(12)}_{m_2 m_2,n_1 n_1}(\omega) + C''^{(22)}_{n_1 n_1,n_2 n_2}(\omega)$$
$$+ C''^{(12)}_{k_2 k_2 n_1 n_1}(\omega) + C''^{(22)}_{n_1 n_1,l_2 l_2}(\omega) + C''^{(11)}_{k_1 k_1,m_2 m_2}(\omega) + C''^{(12)}_{k_1 k_1,n_2 n_2}(\omega) + C''^{(11)}_{k_1 k_1,k_2 k_2}(\omega)$$
$$+ C''^{(12)}_{k_1 k_1,l_2 l_2}(\omega) + C''^{(12)}_{m_2 m_2,l_1 l_1}(\omega) + C''^{(22)}_{l_1 l_1,n_2 n_2}(\omega) + C''^{(12)}_{k_2 k_2,l_1 l_1}(\omega) + C''^{(22)}_{l_1 l_1,l_2 l_2}(\omega)]. \quad (A3)$$

[1] R. E. Blankenship, *Molecular Mechanisms of Photosynthesis* (Blackwell Science Ltd, Oxford, 2002).

[2] G. Renger and T. Renger, Photosynth. Res. **98**, 53 (2008).

[3] A. Guskov, J. Kern, A. Gabdulkhakov, B. M. A. Zouni, and W. Saenger, Nat. Struct. Mol. Biol. **16**, 334 (2009).

[4] H. van Amerogen, L. Valkunas, and R. van Grondelle, *Photosynthetic Excitons* (World Scientific, Singapore, 2000).

[5] G. Raszewski, B. A. Diner, E. Schlodder, and T. Renger, Biophys. J. **95**, 105 (2008).

[6] V. Novoderezhkin, J. Dekker, H. van Amerongen, and R. van Grondelle, Biophys. J. **93**, 1293 (2007).

[7] V. I. Novoderezhkin, M. A. Palacios, H. van Amerongen, and R. van Grondelle, J. Phys. Chem. B **109**, 10493 (2005).

[8] W. M. Zhang, T. Meier, V. Chernyak, and S. Mukamel, J. Chem. Phys. **108**, 7763 (1998).

[9] T. van Voorhis, T. Kowalczyk, B. Kaduk, L.-P. Wang, C.-L. Cheng, and Q. Wu, Annu. Rev. Phys. Chem. **61**, 149 (2010).

[10] H. Haug and S. W. Koch, *Quantum Theory of the Optical and Electronic Properties of Semiconductors*, 4th ed. (World Scientific, Singapore, 2004).

[11] T. Meier, P. Thomas, and S. W. Koch, *Coherent Semiconductor Optics: From Basic Concepts to Nanostructure Applications* (Springer, Berlin, Heidelberg, 2006).

[12] D. Abramavicius, B. Palmieri, D. V. Voronine, F. Šanda, and S. Mukamel, Chem. Rev. (Washington, D.C.) **109**, 2350 (2009).

[13] N. G. van Kampen, *Stochastic Processes in Physics and Chemistry*, 3rd ed. (Elsevier, Amsterdam, 2007).

[14] T. Renger, Phys. Rev. Lett. **93**, 188101 (2004).

[15] T. Mancal, L. Valkunas, and G. R. Fleming, Chem. Phys. Lett. **432**, 301 (2006).

[16] E. Collini and G. D. Scholes, Science **323**, 369 (2009).

[17] B. Palmieri, D. Abramavicius, and S. Mukamel, J. Chem. Phys. **130**, 204512 (2009).

[18] D. Abramavicius and S. Mukamel, J. Chem. Phys. **133**, 064510 (2010).

[19] A. G. Redfield, IBM J. Res. Dev. **1**, 19 (1957).

[20] T. Förster, Annalen der Physik. **437**, 55 (1948).

[21] M. Yang and G. R. Fleming, Chem. Phys. **282**, 163 (2002).

[22] S. Mukamel and V. Rupasov, Chem. Phys. Lett. **242**, 17 (1995).

[23] R. A. Marcus, J. Phys. Chem. **67**, 853 (1963).

[24] S. Mukamel, *Principles of Nonlinear Optical Spectroscopy* (Oxford University Press, New York, 1995).

[25] G. Raszewski and T. Renger, J. Am. Chem. Soc. **130**, 4431 (2008).

[26] G. Raszewski, W. Saenger, and T. Renger, Biophys. J. **88**, 986 (2005).

[27] R. Simonetto, M. Crimi, D. Sandonà, R. Croce, G. Cinque, J. Breton, and R. Bassi, Biochemistry **38**, 12974 (1999).

[28] V. I. Novoderezhkin, E. G. Andrizhiyevskaya, J. P. Dekker, and R. van Grondelle, Biophys. J. **89**, 1464 (2005).

[29] See supplementary material at http://dx.doi.org/10.1063/1.3493580 for the full list of the double-exciton states in molecular basis set.

[30] D. Abramavicius, D. V. Voronine, and S. Mukamel, Proc. Natl. Acad. Sci. U.S.A. **105**, 8525 (2008).

[31] D. Abramavicius, L. Valkunas, and S. Mukamel, Europhys. Lett. **80**, 17005 (2007).

[32] I. V. Schweigert and S. Mukamel, Phys. Rev. A **77**, 033802 (2008).

[33] D. Abramavicius, D. V. Voronine, and S. Mukamel, Biophys. J. **94**, 3613 (2008).

[34] D. Abramavicius, B. Palmieri, and S. Mukamel, Chem. Phys. **357**, 79 (2009).

[35] D. Abramavicius and S. Mukamel, J. Phys. Chem. B **113**, 6097 (2009).

[36] T. Mančal, A. Nemeth, F. Milota, V. Lukeš, H. F. Kauffmann, and J. Sperling, J. Chem. Phys. **132**, 184515 (2010).

[37] D. Abramavicius and L. Valkunas, Phys. Rev. B **68**, 245203 (2003).

[38] D. Abramavicius, L. Valkunas, and R. van Grondelle, Phys. Chem. Chem. Phys. **6**, 3097 (2004).